Journal of Computational Physics 227 (2008) 10226–10242

Contents lists available at ScienceDirect

Journal of Computational Physics

journal homepage: www.elsevier.com/locate/jcp

A discontinuous Galerkin method for the shallow water equations in spherical triangular coordinates ☆

Matthias Läuter [a,*], Francis X. Giraldo [b], Dörthe Handorf [a], Klaus Dethloff [a]

[a] Alfred Wegener Institute for Polar and Marine Research in the Helmholtz Association, P.O. Box 60 01 49, 14401 Potsdam, Germany
[b] Naval Postgraduate School, Department of Applied Mathematics, Spanagel Hall 253A, 833 Dyer Road, Monterey, CA 93943-5216, USA

ARTICLE INFO

Article history:
Received 31 October 2007
Received in revised form 26 August 2008
Accepted 26 August 2008
Available online 5 September 2008

Keywords:
Finite elements
Finite volumes
Shallow water equations
Triangular grid
Spherical geometry
Surface

ABSTRACT

A global model of the atmosphere is presented governed by the shallow water equations and discretized by a Runge–Kutta discontinuous Galerkin method on an unstructured triangular grid. The shallow water equations on the sphere, a two-dimensional surface in $\mathbb{R}^3$, are locally represented in terms of spherical triangular coordinates, the appropriate local coordinate mappings on triangles. On every triangular grid element, this leads to a two-dimensional representation of tangential momentum and therefore only two discrete momentum equations.

The discontinuous Galerkin method consists of an integral formulation which requires both area (elements) and line (element faces) integrals. Here, we use a Rusanov numerical flux to resolve the discontinuous fluxes at the element faces. A strong stability-preserving third-order Runge–Kutta method is applied for the time discretization. The polynomial space of order k on each curved triangle of the grid is characterized by a Lagrange basis and requires high-order quadature rules for the integration over elements and element faces. For the presented method no mass matrix inversion is necessary, except in a preprocessing step.

The validation of the atmospheric model has been done considering standard tests from Williamson et al. [D.L. Williamson, J.B. Drake, J.J. Hack, R. Jakob, P.N. Swarztrauber, A standard test set for numerical approximations to the shallow water equations in spherical geometry, J. Comput. Phys. 102 (1992) 211–224], unsteady analytical solutions of the nonlinear shallow water equations and a barotropic instability caused by an initial perturbation of a jet stream. A convergence rate of $O(\Delta x^{k+1})$ was observed in the model experiments. Furthermore, a numerical experiment is presented, for which the third-order time-integration method limits the model error. Thus, the time step Δt is restricted by both the CFL-condition and accuracy demands. Conservation of mass was shown up to machine precision and energy conservation converges for both increasing grid resolution and increasing polynomial order k.

1. Introduction

Modeling atmospheric flows for climate simulations as well as for weather prediction is a complex problem, due to the nonlinear structure of the dynamical and physical phenomena on widely varying spatial and temporal scales and their multi-scale interaction processes. Depending on the complexity of an atmospheric model the governing equations are the fundamental atmospheric conservation laws for mass, momentum, and energy or appropriate simplifications of them. If

☆ This work relates to Department of the Navy Grant N00014-07-1-4038 issued by the Office of Naval Research Global. The United States Government has a royalty-free licence throughout the world in all copyrightable material contained herein.

* Corresponding author. Tel.: +49 3312882153; fax: +49 3312882178.
E-mail address: Matthias.Laeuter@awi.de (M. Läuter).

0021-9991/$ - see front matter © 2008 Elsevier Inc. All rights reserved.
doi:10.1016/j.jcp.2008.08.019

the regarded equation set is a hyperbolic system, energetic shocks can develop theoretically. Although this is usually not the case in atmospheric models, the discretization should represent regions of scale collapse and breaking waves generating discontinuities in the velocity field; the discrete conservation properties of the discontinuous Galerkin (DG) method are appropriate for this task.

The shallow water equations (SWE), valid for a homogeneous atmosphere with small vertical velocities and horizontal velocities independent in the vertical direction, constitute a hyperbolic system of conservation laws. It is one of the simplest nonlinear hyperbolic systems, covering important planetary atmospheric features, like the Rossby wave formation.

For the spherical SWE the spatial domain is the sphere S, a two-dimensional surface in $\mathbb{R}^3$. In a regional or mesoscale SWE model the momentum is a two-dimensional vector. In contrast, the Cartesian formulation of the spherical case in [43,8,44] represents the tangential momentum of the flow as a three-dimensional vector and includes a Lagrangian multiplier to constrain the momentum to be tangential. Applying this form to a numerical model usually leads to three momentum equations and requires a correction step to satisfy the constraint discretely, see e.g. [17]. Models in standard spherical coordinates satisfy a two-dimensional momentum representation but have to pay additional attention to phenomena near the poles due to singularities of the coordinate mapping, see e.g. [27].

The idea to avoid the drawbacks of the Cartesian and the spherical coordinates formulation is to represent the spherical SWE in terms of local coordinate transformations. On a cubed-sphere grid, a spherical quadrilateral grid, the following works [37,33,31,45,35] achieved a two-dimensional momentum representation avoiding any pole problem. Our new model achieves the same flexibility but on unstructured triangular grids using spherical triangular coordinates.

Numerous models on spherical triangles have been proposed in the last three decades. For example, the early work by Sadourny at al. [38] and Williamson [49] introduced to the atmospheric community the use of triangular grids based on the icosahedron to develop the underlying grid for the construction of finite difference operators. Work on triangular grids based on the icosahedron for discretizing the sphere lay dormant for another 15 years until the work was resumed by Baumgardner and Frederickson [1]. Ten years later work on these grids was resurrected by Heikes and Randall [20] and followed by Giraldo [13], Thuburn [47], Stuhne and Peltier [42], Tomita et al. [48], and Heinze and Hense [21]. All of these models rely directly on either the triangular grid being derived from the icosahedron or on a linear representation of the discrete operators; this way there is an easily computable dual grid which is based on hexagons (icosahedron) or the operators can be constructed using the vertices of an element which are co-planar (linear representation). However, for high-order operators on general triangular grids, one needs to construct the discrete spatial operators directly on the curved manifold which then requires the derivation of the Christoffel symbols from differential geometry (see [35] for a summary of the use of differential geometry for atmospheric flow).

One of the contributions of this manuscript is to show how to use these ideas for constructing high-order spatial operators on general triangulations on the sphere. While these ideas have been used extensively for quadrilateral-based grids, they have not been used at all (or not often); to our knowledge, there are currently no existing models on the sphere which use high-order discretizations on the triangle with the exception being those developed by the present authors. Läuter et al. [25] developed a shallow water model on the sphere using second order finite elements on dynamically adaptive triangular grids, while Giraldo and Warburton [17] and Giraldo [15] developed shallow water models on the sphere using up to 15 order spectral element and discontinuous Galerkin operators on unstructured triangular grids. Extracting the highlights of these three separate works results in a robust, accurate, and efficient model. However, in order to achieve this aim requires writing the equations directly on the parametric space defined by the curved spherical triangles. We consider the spherical SWE in flux form on the surface S using coordinate independent differential operators on S known from differential geometry. By using an appropriate local coordinate mapping γ_E on the curved spherical triangle E we can then obtain a two-dimensional representation of the tangential momentum vectors. This then allows us full grid independence such that our discrete operators can be constructed to arbitrarily high-order while doing so on generalized unstructured triangulations on the sphere (or any other curved manifold, for that matter). This approach allows us the same flexibility enjoyed with the Cartesian methods discussed previously while now only requiring tangential momentum equations.

Numerous numerical methods have been proposed for next generation global atmospheric models including finite volumes [27,34], spectral elements [45,11,9,17], and DG [16,30,15] methods. We have selected the DG method for our model because it allows us to achieve high-order accuracy as in spectral elements while conserving all quantities both locally and globally as in finite volumes, see the review in [5]. Furthermore, our use of unstructured triangular grids allows for much flexibility in future work on adaptivity.

The organization of this article is as follows. In Section 2 the governing spherical SWE are given using surface differential operators. Section 3 describes the numerical discretization by a Runge–Kutta discontinuous Galerkin method applying spherical triangular coordinates. In Section 4 the atmospheric model based on the discretization is validated in terms of standard tests from Williamson et al. [50], steady-state and unsteady analytical solutions and a barotropic instability generated by a small initial perturbation.

2. Spherical shallow water equations

The spherical SWE are a system of conservation laws for the geopotential layer depth (mass) and the flow momentum. Because the integration domain of the SWE is the sphere, a two-dimensional surface in $\mathbb{R}^3$, the system can be formulated

in the surrounding Cartesian space $\mathbb{R}^3$, see Côté [8]. Côté's formulation is equivalent to a conservative form of the SWE on the surface S, which is the formulation used further below.

Let us consider the sphere $S = \{x \in \mathbb{R}^3 | |x| = a\}$ with the Earth's radius $a = 6.371 \times 10^6$ m, the geopotential layer depth $\Phi : S \times \mathbb{R}_{\geqslant 0} \to \mathbb{R}$, the tangential momentum field $U : S \times \mathbb{R}_{\geqslant 0} \to \mathbb{R}^3$ with $U(x,t) \in T_x(S)$ and the conserved variable $q = (\Phi, U^T)^T$. Momentum and velocity fulfill the relation $U = \Phi u$. Then, the SWE in conservative form on the surface S are

$$\partial_t q + \operatorname{div}_S f(q) = F(x,q) \quad \text{in } S \times \mathbb{R}_{\geqslant 0}. \tag{1}$$

Thereby, the flux function and the right hand side are

$$f(q) = \begin{pmatrix} f_\Phi(q) \\ f_U(q) \end{pmatrix}, \quad f_\Phi(q) = U, \quad f_U(q) = \frac{U \otimes U}{\Phi} + \frac{\Phi^2}{2} \mathrm{Id}_3,$$
$$F(x,q) = \begin{pmatrix} 0 \\ F_U(x,q) \end{pmatrix}, \quad F_U(x,q) = -f_c k \times U - \Phi \nabla_S \Phi_B - \frac{U^2}{\Phi a} k$$

with the Earth's angular velocity $\Omega = 7.292 \times 10^{-5}$ s^{-1}, the space dependent Coriolis parameter $f_c(x) = 2\Omega \frac{x \cdot e_3}{|x|}$, the geopotential bottom height $\Phi_B : S \to \mathbb{R}$. Further, the normal unit vector $k(x) = \frac{x}{|x|}$ outward on S, the identity mapping Id_3 in $\mathbb{R}^3$ and the Cartesian basis $(e_i)_{i=1,2,3}$ of $\mathbb{R}^3$ are defined. See Appendix for the definition of the differential operators on S.

As a consequence of (1), mass is locally and globally conserved, energy is globally conserved and for $\Omega = \Phi_B = 0$ angular momentum is globally conserved, see [29]. Three prognostic equations for the momentum Φu appear in (1), whereas the momentum is forced to be tangential on S by the Lagrangian multiplier $-\frac{U^2}{\Phi a} k$. Although this pseudo force has no physical origin, in the spherical system it is a perturbation for the global conservation of momentum. Of course without that pseudo force (and $\Omega = \Phi_B = 0$), like for the two-dimensional shallow water equations, conservation of momentum is obtained.

3. Discontinuous Galerkin method

The DG method is applied to the conservative form (1) of the SWE on the surface S. On each curved triangle (element) E of the grid tesselation spherical triangular coordinates are introduced, which are local coordinate mappings γ_E on E. The polynomial representation on each grid element uses high-order Lagrange polynomials based on specially chosen Lagrange points (see Section 3.2). This approach leads to the local representation of the tangential momentum fields by two components only. An integral form of (1) leads to the space-discrete DG method including a Rusanov numerical flux. For this method high-order quadrature rules are applied and, except in a preprocessing step, no mass matrix inversion has to be evaluated. Finally the semi-discrete problem is solved by a strong stability-preserving explicit Runge–Kutta (RK) method. Although slope limiting steps are needed to prove convergence in the one-dimensional scalar case (see [5]) the presented RK-DG method avoids any kind of limiting or explicit smoothing such as diffusion and filter operators. Nevertheless for the performed numerical experiments, this method gives stable results (see Section 4).

3.1. Spherical triangular coordinates

Let $E \subset S$ be a relative open spherical triangle bounded by great circles and defined by its vertices $x_0, x_1, x_2 \in S$. Then we define for E the local coordinate mapping γ_E, or the spherical triangular coordinates, by

$$\gamma_E : D \to E, \gamma_E(y) = a \frac{x_p(y)}{|x_p(y)|}. \tag{2}$$

Here, $D = \{y \in \mathbb{R}^2 | 0 < y_1, y_2; y_1 + y_2 < 1\}$ is a two-dimensional reference triangle, and $x_p(y) = x_0 + y_1(x_1 - x_0) + y_2(x_2 - x_0)$ an auxiliary planar mapping. Following the notation in Appendix, a basis of $T_x(S)$, Gram's determinant and the Christoffel symbols are given with $i, j, k = 1, 2$

$$b_i = \frac{a}{|x_p|} \left((x_i - x_0) - (x_i - x_0) \cdot \frac{x_p}{|x_p|} \frac{x_p}{|x_p|} \right),$$
$$g = (b_1 \times b_2)^2, \quad \Gamma^i_{jk} = -\frac{x_p}{x_p^2} \cdot ((x_j - x_0)\delta^i_k + (x_k - x_0)\delta^i_j).$$

3.2. Discrete function space

Let $\mathcal{T} = \{E \subset S | E \text{ spherical triangle}, E \text{ open in } S\}$ be a finite conformal triangulation of the sphere – that is, a triangular grid without hanging nodes. For the presented model, $\mathcal{T}$ is constructed by the grid generator AMATOS, see [2]. Dependent on the grid level l, an icosahedral coarse grid $\mathcal{T}_0$ is refined in l steps, in which every triangle of $\mathcal{T}_0$ is divided by bisection. This leads to an unstructured spherical triangulation $\mathcal{T}$ with reasonably uniform grid resolution, see Fig. 1.

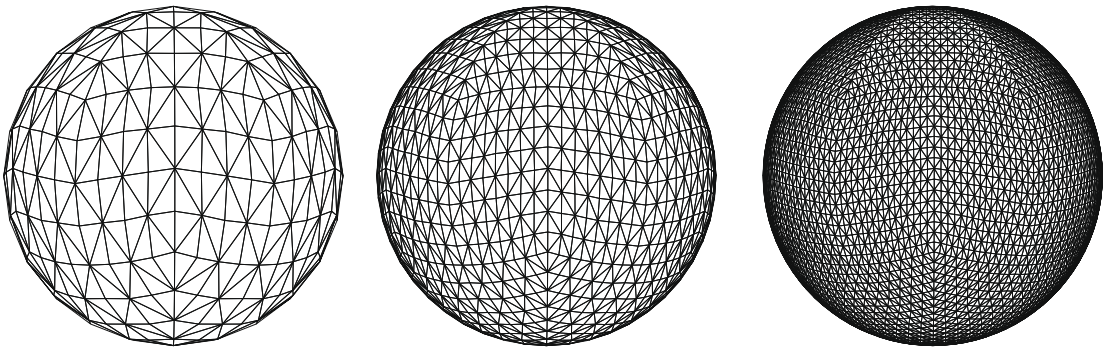

Fig. 1. Section 3.2, uniform grid, grid resolution 2058 km (left), 1041 km (middle), 522 km (right).

The polynomial space of the polynomials of degree at most $k \geqslant 0$ on every element $E \in \mathcal{T}$ is defined by

$$P^k(E) = \{\varphi : E \to \mathbb{R} | \varphi \circ \gamma_E \in P^k(D)\}, \text{with}$$
$$P^k(D) = \text{span}\{p_{ij} : D \to \mathbb{R} | i,j = 0,\ldots,k; i+j \leqslant k; \quad p_{ij}(y_1,y_2) = y_1^i y_2^j\}$$

and γ_E is the spherical triangular coordinate mapping (2). Thus, the coordinate mapping γ_E defines both the curved geometry of E and the polynomial space on E. This technique for curved elements is similar to the definition of isoparametric finite elements, see [3], but with an analytically non-polynomial mapping γ_E.

Every polynomial $p \in P^k(E)$ is represented by a multivariate Lagrange basis $(\varphi_i)_{i=1,\ldots,N_k}$ of $P^k(E)$, with $N_k = \frac{(k+1)(k+2)}{2}$, associated with the Lagrange points $(x_i)_{i=1,\ldots,N_k}$, that is for $x \in E$

$$p(x) = \sum_{i=1}^{N_k} \varphi_i(x) p(x_i). \tag{3}$$

Thereby, $(x_i)_{i=1,\ldots,N_k}$ as well as $(\varphi_i)_{i=1,\ldots,N_k}$ are defined by $\varphi_i = \tilde{\varphi}_i \circ \gamma_E^{-1}$ and $x_i = \gamma_E(\tilde{x}_i)$. $(\tilde{\varphi}_i)_{i=1,\ldots,N_k}$ is the multivariate Lagrange basis of $P^k(D)$ associated with the electrostatic points $(\tilde{x}_i)_{i=1,\ldots,N_k}$ in D derived from the electrostatics principle. These points have the smallest Lebesgue constants for $k < 9$ and are the result of numerical studies minimizing a certain energy function, see [22]. Another appropriate choice would have been the Fekete points which have only slightly larger Lebesgue constants for $k < 9$ but smaller Lebesgue constants for $k \geqslant 9$, see [46]. Here, we chose electrostatic points because all model experiments in Section 4 are performed with polynomial order $k < 9$.

Based on the polynomial space $P^k(E)$, the discrete discontinuous function spaces for the scalar fields and tangential vector fields are defined by

$$V_\Phi = \{\Phi \in L^\infty(S) | \forall E \in \mathcal{T} : \Phi|_E \in P^k(E)\},$$
$$V_U = \{U \in L^\infty(S,\mathbb{R}^3) | \forall E \in \mathcal{T} : U|_E = U^1 b_1 + U^2 b_2 \text{ with } U^1, U^2 \in P^k(E)\},$$
$$V_U^* = \{U \in L^\infty(S,\mathbb{R}^3) | \forall E \in \mathcal{T} : U|_E = U_1 b^1 + U_2 b^2 \text{ with } U_1, U_2 \in P^k(E)\}.$$

Because $\Phi \in V_\Phi, U \in V_U, V \in V_U^*$ are polynomials on each grid element E, the condition $\Phi, U, V \in L^\infty$ does not constitute an additional constraint to the discrete functions. The function spaces V_U and V_U^* contain tangential vector fields, that is $U(x) \in T_x(S)$ for $U \in V_U \cup V_U^*$. For every momentum $U \in V_U$ the restriction $U|_E$ is a vector field having polynomial components with respect to b_1 and b_2. Test functions for the momentum equation are to be vector fields $U \in V_U^*$ where their restriction $U|_E$ has polynomial components with respect to the dual basis b^1 and b^2.

Remark 1. The discrete function spaces V_U and V_U^* for the tangential vector fields incorporating spherical triangular coordinates ensure the two-dimensional representation of the momentum in (1). This denotes a reduction compared to the three-dimensional representation in the Cartesian coordinate system used in [15,17]. Further, this approach avoids any kind of projection step incorporating a discrete version of the Lagrangian multiplier in the numerical scheme.

3.3. Space-discrete formulation

The starting point for the space-discrete formulation is an approriate integral form of the conservation law. This is obtained multiplying (1) with a smooth (continuous in S with derivatives) test function $p = (\varphi, V)^T$, assuming a smooth solution q of (1), integrating over $E \in \mathcal{T}$ and applying (10), that is

$$\int_E (p \cdot \partial_t q - f(q) : \nabla_S p) \mathrm{d}x + \int_{\partial E} p \cdot f(q) \cdot \nu_E \mathrm{d}\sigma = \int_E p \cdot F(x,q) \mathrm{d}x.$$

Here $f(q) : \nabla_S p = f_\Phi(q) \cdot \nabla_S \varphi + \sum_{i=1}^{3} e^i \cdot f_U(q) \cdot \nabla_S (V \cdot e_i)$ and ν_E is the normal unit vector outward on ∂E. This integral form of (1) is to be the condition that the space-discrete solution $q_h(t) \in V_\Phi \times V_U$ has to fulfill, that is

$$\begin{aligned} &\forall p \in V_\Phi \times V_U^*, \quad \forall E \in \mathcal{T} \\ &\int_E (p \cdot \partial_t q_h - f(q_h) : \nabla_S p) \mathrm{d}x + \int_{\partial E} p^{\mathrm{in}} \cdot \hat{f}_E(x, q_h^{\mathrm{in}}, q_h^{\mathrm{out}}) \mathrm{d}\sigma = \int_E p \cdot F(x, q_h) \mathrm{d}x. \end{aligned} \tag{4}$$

By means of the discrete equation, q_h as well as the test functions p are in discrete function spaces. The function space V_U^* is used for V instead of V_U to simplify the discrete representation (6) of (4). Further, due to the discontinuities of $q_h = (\Phi, U) = (\Phi, \Phi u)$ along the edges of the triangles, the values of the flux function $f(q_h)$ are not defined on the boundaries ∂E. That is why, in the boundary integral of (4), the flux $f(q_h)$ is replaced by the Rusanov numerical flux

$$\hat{f}_E(x, q_h^{\mathrm{in}}, q_h^{\mathrm{out}}) = \frac{1}{2}[(f(q_h^{\mathrm{in}}) + f(q_h^{\mathrm{out}})) \cdot \nu_E(x) - \lambda(q_h^{\mathrm{out}} - q_h^{\mathrm{in}})],$$

with the maximum wave speed $\lambda = \max(|u^{\mathrm{in}} \cdot \nu_E| + \sqrt{\Phi^{\mathrm{in}}}, |u^{\mathrm{out}} \cdot \nu_E| + \sqrt{\Phi^{\mathrm{out}}})$ in system (1). Below the notation $\hat{f}_E = (\hat{f}_\Phi, \hat{f}_U)^T$ regarding the scalar and momentum components will be used.

To obtain a matrix formulation of (4), the decomposition $q_h = (\Phi, U)$ with $\Phi \in V_\Phi$ and $U \in V_U$ is regarded. Using the decomposition (3) with regards to the Lagrange basis in $E \in \mathcal{T}$ yields

$$\Phi(x,t) = \sum_{i=1}^{N_k} \Phi_i(t) \varphi_i(x), \quad U(x,t) = \sum_{i=1}^{N_k} \sum_{l=1}^{2} U_i^l(t) \varphi_i(x) b_l(x),$$

the representation of q_h in E in terms of its component vector

$$\hat{q}_{h,E} = (\Phi_1, \ldots, \Phi_{N_k}, \quad U_1^1, \ldots, U_{N_k}^1, \quad U_1^2, \ldots, U_{N_k}^2), \quad \hat{q}_h = (\hat{q}_{h,E})_{E \in \mathcal{T}}.$$

As expected, the tangential momentum field U in E is represented by the last $2N_k$ components of $\hat{q}_{h,E}$ only. Then, q_h is a solution of (4) if and only if in every $E \in \mathcal{T}$ for all $j = 1, \ldots, N_k$ and $l = 1, 2$ the following equations hold

$$\sum_{i=1}^{N_k} \frac{\mathrm{d}\Phi_i}{\mathrm{d}t} \int_E \varphi_j \varphi_i \mathrm{d}x - \int_E f_\Phi(q_h) \cdot \nabla_S \varphi_j \mathrm{d}x + \int_{\partial E} \varphi_j \hat{f}_\Phi \mathrm{d}\sigma = 0, \tag{5}$$

$$\sum_{i=1}^{N_k} \frac{\mathrm{d}U_i^l}{\mathrm{d}t} \int_E \varphi_j \varphi_i \mathrm{d}x - \int_E f_U^l \cdot \nabla_S \varphi_j \mathrm{d}x + \int_{\partial E} \varphi_j \hat{f}_U^l \mathrm{d}\sigma = \int_E \varphi_j \tilde{F}_U^l \mathrm{d}x. \tag{6}$$

Here the notation $f_U^l = b^l \cdot f_U(q_h)$, $\hat{f}_U^l = b^l \cdot \hat{f}_U$, $\tilde{F}_U^l = b^l \cdot F_U - \sum_{i,m=1}^{2} f_U^{im} \Gamma_{mi}^l$, $F_U^l = b^l \cdot F_U$, $f_U^{im} = b^i \cdot f_U(q_h) \cdot b^m$ has been used. Using the dual momentum space V_U^* for the test functions in (4) leads to the desirable separation of equations for the momentum components for $(U_i^1)_{i=1,\ldots,N_k}$ and $(U_i^2)_{i=1,\ldots,N_k}$ in (6). Eq. (6), for $l = 1, 2$, are two space-discrete momentum equations, only.

To proceed with the space-discrete system further below Eqs. (5) and (6) are written in the compact form

$$\frac{\mathrm{d}\hat{q}_h}{\mathrm{d}t} = L(\hat{q}_h) \tag{7}$$

with an appropriate right hand side operator L. The evaluation of $L(\hat{q}_h)$ includes the evaluation of integrals over E and ∂E using the representation formulae (11). The integrands include both the flux function f in (1) and the surface geometry represented by Gram's determinant g. In each triangle E quadrature rules of order $2k$ are applied given in [41,7,28,6]. On each edge of E standard Gauss-Lobatto rules of order $2k-1$ are applied, since the electrostatic points are in fact Gauss-Lobatto points along the edges, see [22]. Although [5] indicates, that quadrature rules of order $2k+1$ along the edges are to be used for $k+1$-order formal accuracy, this would slow down the scheme. Experiments with a strong DG method in [15] have shown satisfactory results applying $2k-1$ order quadrature. Furthermore, we rely on the superconvergence property of outflow flux integrals described in [23] to motivate our use of $2k-1$ quadrature for the boundary integrals.

Remark 2. $\hat{f}_E(x, q_h^{\mathrm{in}}, q_h^{\mathrm{out}})$ is a function of space and the conserved variables only, that is $\hat{f}_E$ is independent on the local coordinate mapping γ_E. On the other hand, the formulations (5) and (6) depend on the coordinate mapping γ_E because these determine the components Φ_i and U_i^l regarding the polynomial basis $(\varphi_i)_{1,\ldots,N_k}$ of $P^k(E)$.

Remark 3. If the triangulation $\mathcal{T}$ is time independent, the mass matrix entries $M_{ij} = \int_E \varphi_j \varphi_i \mathrm{d}x$ can be pre-evaluated once. Thus, multiplying (5) and (6) by M^{-1} leads to the substitution of φ_j and $\nabla_S \varphi_j$ by $M_{ij}^{-1} \varphi_j$ and $M_{ij}^{-1} \nabla_S \varphi_j$, respectively. The resulting equations allow the evaluation of $\partial_t \hat{q}_h$ avoiding any runtime mass matrix inversion.

3.4. Runge–Kutta method

A strong stability-preserving (SSP) explicit third-order Runge–Kutta (RK) method, see [19], is used to solve the ordinary differential Eq. (7), that is for every time step $t^n \to t^{n+1}$

$$q^{(0)} = q_{\mathrm{h}}^{n}, \quad q^{(i)} = q^{(0)} + \tau \sum_{j=0}^{i-1} c_{ij} L(q^{(j)}), \quad i = 1, \ldots, s$$
$$q_{\mathrm{h}}^{n+1} = q^{(s)}, \tag{8}$$

where $s = 3$,

$$(c_{10}, c_{20}, c_{21}, c_{30}, c_{31}, c_{32}) = \left(1, \frac{1}{2}, \frac{1}{4}, \frac{1}{2}, \frac{1}{6}, \frac{2}{3}\right). \tag{9}$$

SSP methods combine high-order accuracy with stability properties respecting a CFL-condition. For nonlinear scalar conservation laws in one space-dimension [39] showed, that if the forward Euler method is total variation diminishing (TVD), then (8) is TVD with an appropriate CFL-condition, too. Although this does not prove stability for (8) applied to (7), it gives a good indication that this SSP method is not a source of spurious oscillations in the discrete solution.

For a given polynomial degree k in Section 3.2 a SSP method of order $k+1$ would be desirable. Only a third-order method (9) has been chosen, because SSP-RK methods with positive coefficients of order higher than four do not exist, see [36]. Further, there is no 4-stage 4th-order SSP-RK method with non-negative coefficients, see [19]. All numerical experiments in Section 4 show stable results even for $k > 2$.

4. Numerical results

The RK-DG method described in Section 3 has been used to implement an atmospheric model which has been validated performing numerical experiments. The validation process is carried out in three steps. At first, standard model tests (flow over an isolated mountain and a Rossby–Haurwitz wave) from Williamson [50] are performed. After that, a convergence study considering steady-state and unsteady analytical solutions of the nonlinear SWE is done. Finally, a barotropic instability in a localized jet stream has been carried out.

The experiments without a known analytical solution are validated with respect to their properties to conserve the global invariants mass and energy. These are defined by

$$\int_S \Phi_{\mathrm{h}} \mathrm{d}\sigma, \; E_{\mathrm{h}} = \frac{1}{2g} \int_S \frac{U_{\mathrm{h}} \cdot U_{\mathrm{h}}}{\Phi_{\mathrm{h}}} + \Phi_{\mathrm{h}}(\Phi_{\mathrm{h}} + 2\Phi_{\mathrm{B}}) \mathrm{d}\sigma,$$

respectively. As a consequence of the DG method (5), mass is expected to remain constant for each experiment. The relative error of the discrete value E_{h} is computed with respect to the initial value, namely

$$\eta(E_{\mathrm{h}}) = \frac{|E_{\mathrm{h}} - E_{\mathrm{h}}|_{t=0}|}{E_{\mathrm{h}}|_{t=0}}.$$

For the tests with an analytical solution $q = (\Phi_{ana}, \Phi_{ana} u_{ana})^{\mathrm{T}}$, the numerical error is evaluated using the normalized L^2-error of the geopotential field Φ_{h}, that is

$$\eta(\Phi_{\mathrm{h}}) = \frac{\|\Phi_{ana} - \Phi_{\mathrm{h}}\|_{L^2(S)}}{\|\Phi_{ana}\|_{L^2(S)}}.$$

For every element E a local grid resolution Δx_{E} which is the size of the largest edge in E, and a local model resolution h_{E} is defined by $h_{\mathrm{E}} = \sqrt{|E|/N_k}$. The grid resolution Δx and the model resolution h arise from the corresponding maximum values over all elements. Table 1 contains h and the number of grid unknowns, depending on Δx and the polynomial order k.

For linear equations in one dimension, L^2-stability is achieved respecting the CFL-condition

$$\lambda \frac{\Delta t}{\Delta x} \leqslant \frac{1}{2k+1}.$$

While [4] has proven this for $k = 1$, the general case $k \geqslant 2$ is based on numerical experiments, see [5]. For the presented model, one possible generalization is of the type

$$\lambda_{\mathrm{E}} \frac{\Delta t_{\mathrm{E}}}{h_{\mathrm{E}}} = CFL, \quad \Delta t \leqslant \Delta t_{CFL} = \min_{E \in \mathcal{T}} \Delta t_{\mathrm{E}},$$

Table 1
The model resolution h (km)/number of grid unknowns are functions of the grid resolution Δx (km) (left vertical) and the polynomial order k (top horizontal)

Δx (km)/k	2	4	6	8
2058			174/17,920	137/28,800
1041	188/15,360	119/38,400	87/71,680	69/115,200
522	94/61,440	60/153,600	44/286,720	
261	47/245,760	30/614,400		

where λ_E is the characteristic wave speed $\lambda_E = |u| + \sqrt{\Phi}$. The result of our numerical sensitivity experiments is $CFL = \frac{1}{4}$. Rearranging this condition in terms of $\Delta x_E \approx \sqrt{|E|}/2$ gives

$$\lambda_E \frac{\Delta t_E}{\Delta x_E} \approx \frac{1}{\sqrt{2(k+1)(k+2)}}.$$

For the case $k = 2$, the right hand side of this condition yields $\frac{1}{\sqrt{24}}$ which agrees with Cockburns condition $\frac{1}{5}$ very well. The critical time step length Δt_{CFL} is derived in every time step, for given values h_E and λ_E. All numerical experiments, except Section 4.4, have been performed with the time step $\Delta t = \Delta t_{CFL}$. Due to accuracy limitations the smaller time step $\Delta t = \frac{\Delta t_{CFL}}{4}$ is used for the experiments in Section 4.4.

4.1. Isolated mountain test

The first test for the model validation is a quasi-standard test without a known analytical solution. Test 5 in [50] contains a geostrophic balanced solid body rotation which is perturbed by an isolated mountain at 30° north. Rossby waves are generated and propagate to both hemispheres. Fig. 2 shows a snapshot of the geopotential height after an integration time of 15 days.

Due to the lack of an analytical solution, for this experiment the discrete properties of the global invariants mass and energy are inspected. The experiments for all model resolutions approve the conservation of mass up to machine precision. Fig. 3 shows the relative error for the global energy $\eta(E_h)$ as a function of the model resolution h and simulation time T, respectively. At day 15, the error values $\eta(E_h)$ are in the range of $(7.7 \times 10^{-10}, 4.8 \times 10^{-6})$, even for the coarse model resolution of 180 km. For a fixed grid resolution Δx, a higher polynomial order k reduces the error. An error reduction is observed as well for all fixed polynomial orders $k \leqslant 6$ and a decreasing grid spacing Δx (i.e., increasing grid resolution). For the high-order case $k = 8$ the error remains almost constant which may be caused by the non smooth shape of the mountain. The time evolution of the error $\eta(E_h)$ is a monotone increasing function of time which is the anticipated characteristics.

Although the error sensitivity with respect to the model resolution describes the convergence properties, no information about the computational costs is given. For that, Fig. 4 shows the relation between model resolution h and CPU time on a single AMD Opteron machine. The dramatic h^{-3} growth of CPU time is mainly caused by the strong time step limitation due to the CFL condition. This could be improved, e.g. using semi-implicit time stepping to dampen the fast waves, see [10,32]. Because this qualitative characteristics of CPU time is observed also for all the following experiments, this analysis is presented for this test case only.

4.2. Rossby–Haurwitz wave

In test 6 of [50] a transient Rossby–Haurwitz wave is described, which is an analytic solution of the nonlinear barotropic vorticity equation on the sphere. The initial fields with a zonal wave number 4 move in the eastward direction. Although this is not an analytic solution of the SWE, it has been used frequently for model validation. Fig. 5 shows a snapshot of the geopotential height after an integration time of 14 days.

The discrete conservation properties with respect to mass and energy are analyzed. As in Section 4.1, the expected conservation of mass is obtained up to machine precision. Fig. 6 shows the relative error for the global energy $\eta(E_h)$ as a function of the model resolution h and simulation time T, respectively. Compared to Section 4.1, the values of $\eta(E_h)$ reach higher values and range in $(3.0 \times 10^{-8}, 3.7 \times 10^{-5})$. Nevertheless, the experimental convergence with respect to the polynomial order k and to the grid resolution Δx is obtained.

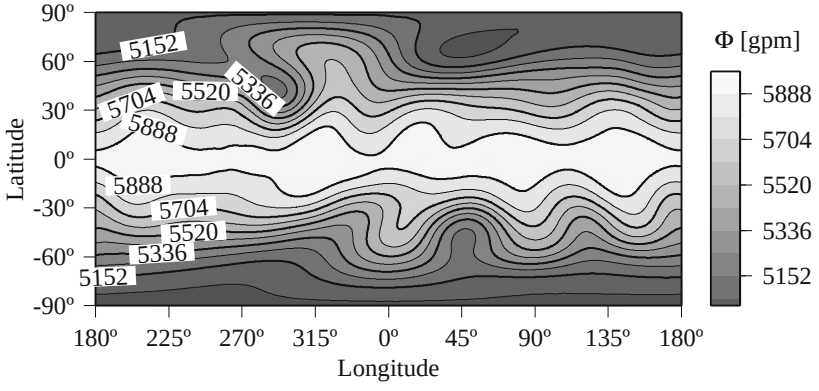

Fig. 2. Section 4.1 (isolated mountain), geopotential height Φ_h after 15 days, $(h, k) = (30\text{ km}, 4)$.

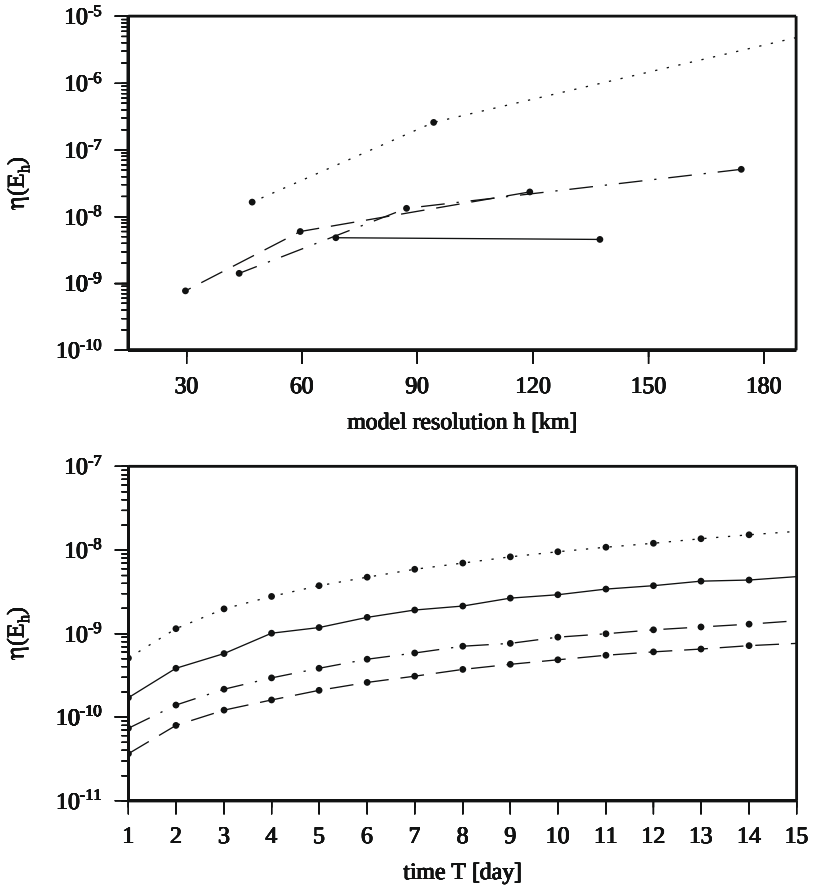

Fig. 3. Section 4.1 (isolated mountain), relative error for global energy $\eta(E_h)$, top: day 15 and $k = 2$ $(\cdots)$, $k = 4$ (–), $k = 6$(-·), $k = 8$ (–), bottom: $(h, k) = (47\text{ km}, 2)$ $(\cdots)$, $(h, k) = (30\text{ km}, 4)$ (–), $(h, k) = (44\text{ km}, 6)$(-·), $(h, k) = (69\text{ km}, 8)$ (–).

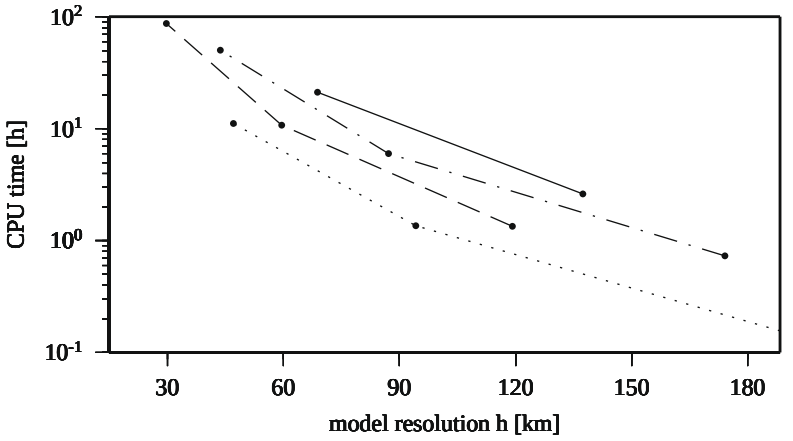

Fig. 4. Section 4.1 (isolated mountain), CPU time in h for 15 days simulation, $k = 2$ $(\cdots)$, $k = 4$ (–), $k = 6$(-·), $k = 8$ (–).

4.3. Steady-state solid body rotation

This test contains a steady-state solution of the nonlinear SWE, see [50, case 2]. The velocity field u is a westerly wind with the meridional distribution of a solid body rotation. The geopotential height Φ is given in geostrophic balance to u. Thus, for the duration of the integration the initial data have to be maintained.

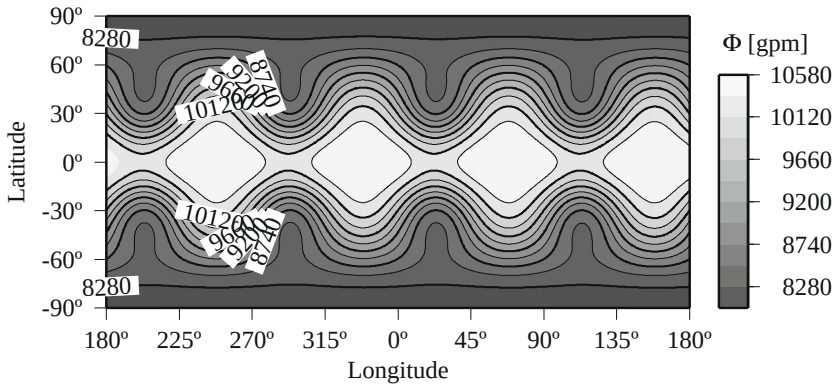

Fig. 5. Section 4.2 (Rossby–Haurwitz wave), geopotential height Φ_h after 14 days, $(h,k) = (30\text{ km},4)$.

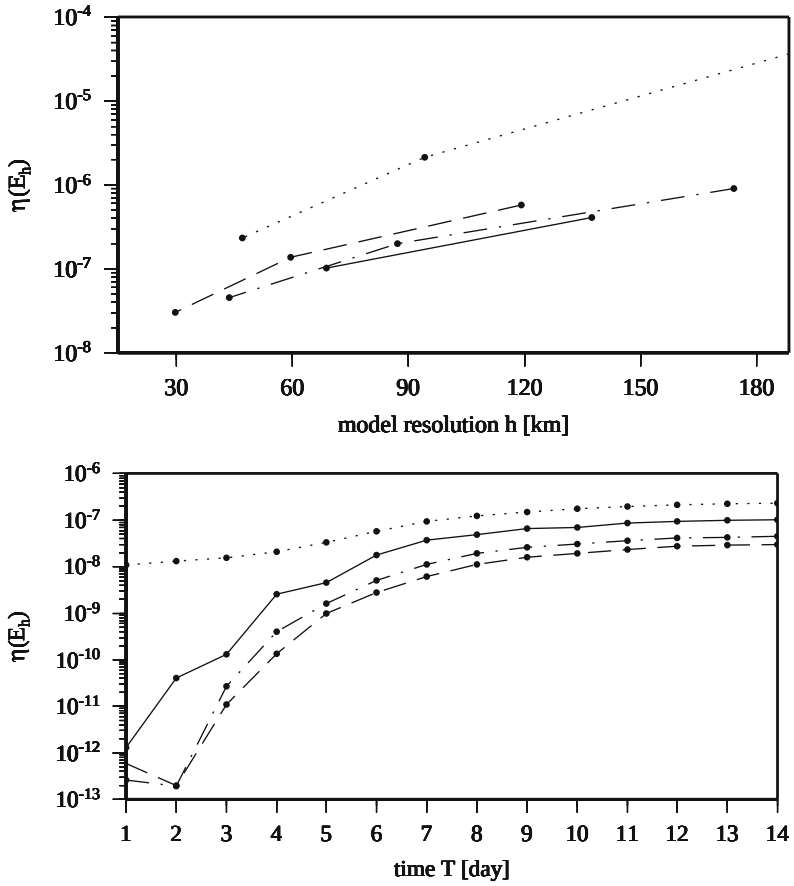

Fig. 6. Section 4.2 (Rossby–Haurwitz wave), relative error for global energy $\eta(E_h)$, top: day 14 and $k = 2$ $(\cdots)$, $k = 4$ (–), $k = 6$(-·), $k = 8$ (–), bottom: $(h,k) = (47\text{ km},2)$ $(\cdots)$, $(h,k) = (30\text{ km},4)$ (–), $(h,k) = (44\text{ km},6)$(-·), $(h,k) = (69\text{ km},8)$ (–).

For the validation, [50] recommend the evaluation of the normalized L^2-error $\eta(\Phi_h)$ after an integration time of 5 days. Fig. 7 shows $\eta(\Phi_h)$ for different polynomial orders $k = 2,4,6,8$ as a function of the model resolution h. For all choices of k the model converges and reduces the error almost up to machine precision for $k = 6,8$. Table 2 shows the expected order of convergence $O(\Delta x^{k+1})$, see [26]. The same experimental order of convergence is obtained by spectral element methods, see [11,18]. Further for fixed grid resolutions Δx, the errors decrease significantly for increasing k. These results are very close to the convergence studies in [16,30,15]. For this steady-state solution no limitation due to the third-order RK method is observable.

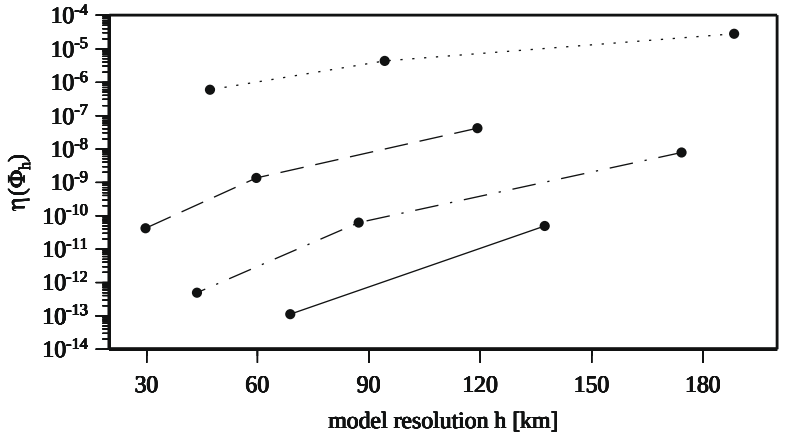

Fig. 7. Section 4.3 (steady-state solid body rotation), normalized L^2-error $\eta(\Phi_h)$ after integration time 5 days as a function of model resolution $h, k = 2$ $(\cdots)$, $k = 4$ $(-)$, $k = 6$ $(-\cdot)$, $k = 8$ $(-)$.

4.4. Unsteady solid body rotation

This test concerns an unsteady solution of the nonlinear SWE, see [24, example 3]. Similar to the last test, the velocity field u is a solid body rotation, but with an inclination to the Earth's rotation axis. The more complex geopotential field is a superposition of two axially symmetric fields. Further, this test requires an axially symmetric orographic field. This analytical solution moves in the westerly direction and has a time period of 1 day.

Again, the normalized L^2-error $\eta(\Phi_h)$ is evaluated after an integration time of 5 days. In this Section the time step is chosen as $\Delta t = \frac{\Delta t_{CFL}}{4}$, which is different from all other numerical experiments in this article. Fig. 8 shows $\eta(\Phi_h)$ for different polynomial orders $k = 2, 4, 6, 8$ as a function of the model resolution h. For all choices of the polynomial order k the model converges, even in this unsteady test case. The errors decrease significantly for increasing k.

For all experiments with small errors $(\eta(\Phi_h) \leqslant 10^{-9})$ the limiting factor for accuracy is the time step Δt and not the model resolution h any more. To see this, Fig. 9 is given, which shows $\eta(\Phi_h)$ as a function of Δt, for fixed parameters (h, k). All exper-

Table 2
Sections 4.3–4.5, Experimental order of convergence for $k = 2, 4, 6, 8$

Test/k	2	4	6	8
Section 4.3	2.86	4.97	6.97	8.78
Section 4.4	3.02	5.02	4.83	4.20
Section 4.5	4.84	5.70	7.25	8.79

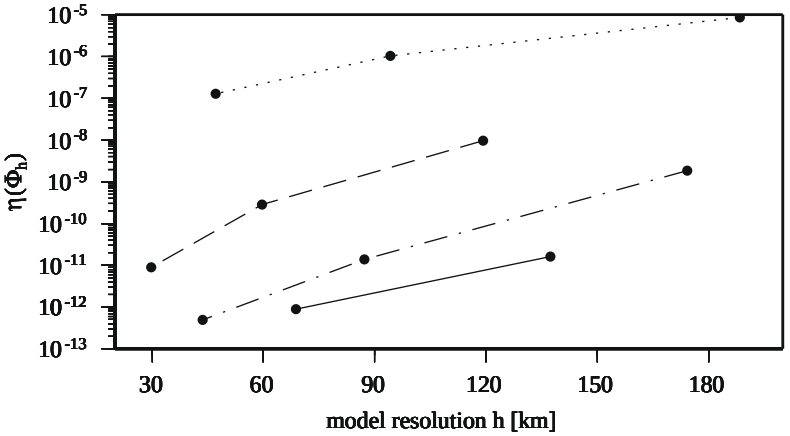

Fig. 8. Section 4.4 (unsteady solid body rotation), normalized L^2-error $\eta(\Phi_h)$ after integration time 5 days as a function of model resolution $h, k = 2$ $(\cdots)$, $k = 4$ $(-)$, $k = 6$ $(-\cdot)$, $k = 8$ $(-)$.

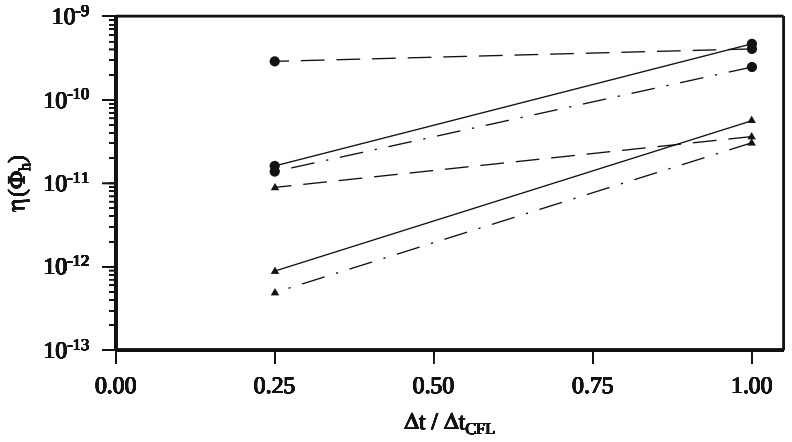

Fig. 9. Section 4.4 (unsteady solid body rotation), normalized L^2-error $\eta(\Phi_h)$ after integration time 5 days as a function of time step $\Delta t/\Delta t_{CFL}$, $(h,k) =$ (60 km,4) (• –), $(h,k) =$ (30 km,4) (▲ –), $(h,k) =$ (87 km,6) (• -·), $(h,k) =$ (44 km,6) (▲ -·), $(h,k) =$ (137 km,8) (•-), $(h,k) =$ (69 km,8) (▲-).

iments which are not plotted in Fig. 9 give the same results independent of the choice of $\Delta t \leqslant \Delta t_{CFL}$. It is to be seen, that $\eta(\Phi_h)$ stagnates for decreasing h, for fixed $\Delta t = \Delta t_{CFL}$ and all experiments with small errors. At the same time, for these experiments Fig. 9 shows $O(\Delta t^3)$ convergence of $\eta(\Phi_h)$. Both observations together yield, once $\eta(\Phi_h)$ is small enough, only a decreasing time step leads to decreasing $\eta(\Phi_h)$. A further error reduction is anticipated for time steps smaller than $\frac{\Delta t_{CFL}}{4}$, which is not shown here due to limited computational resources. Of course this effect could be avoided using an appropriate RK method of order $k+1$. As explained in Section 3.4 a SSP-RK method with a tolerant CFL-condition is not available.

Table 2 shows for $k = 2, 4$ the expected order of convergence $O(\Delta x^{k+1})$. Because for $k = 6, 8$ the convergence is limited by the third-order time step, in this case the convergence rates in space are suboptimal. At the same time the expected third-order accuracy in time can be achieved. Because the absolute L^2-error $\|\Phi_{ana} - \Phi_h\|_{L^2(S)}$ is larger compared to the similar steady-state case in Section 4.3, for the polynomial orders $k = 2, 4, 6$ the normalized error is even smaller. The error for $k = 8$ is limited by the time step, which results in slightly larger errors compared to Section 4.3.

4.5. Unsteady jet stream

This test contains a second unsteady solution of the nonlinear SWE, see [24, example 4]. This time, the velocity field u is an axially symmetric westerly wind jet stream superimposed by a smaller solid body rotation, where the axis of the jet stream is inclined to the Earth's rotation axis. Due to the jet stream strong meridional gradients are present, which presents an additional difficulty compared to Section 4.4. As in Section 4.4, an adequate unsteady geopotential field is available and an axially symmetric orographic field has to be regarded. The solution moves in the westerly direction and has a time period of 1 day.

The normalized L^2-error $\eta(\Phi_h)$ is evaluated after an integration time of 5 days. Fig. 10 shows the normalized L^2-error $\eta(\Phi_h)$ for different polynomial orders $k = 2, 4, 6, 8$ as a function of the model resolution h. The method shows experimental

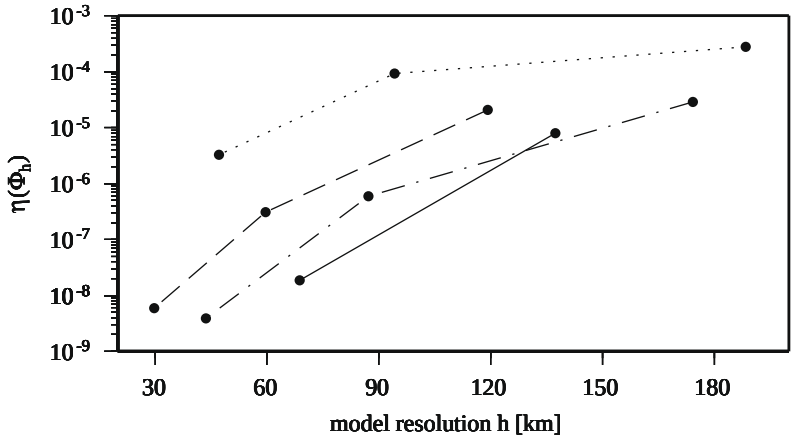

Fig. 10. Section 4.5 (unsteady jet stream), normalized L^2-error $\eta(\Phi_h)$ after integration time 5 days as a function of model resolution $h, k = 2$ (···), $k = 4$ (–), $k = 6$(–·), $k = 8$ (–).

convergence for this test case with strong meridional gradients. For increasing polynomial order k the error $\eta(\Phi_h)$ decreases, but remains significantly larger than in Section 4.4. This is probably the reason for the order of convergence $k+1$, see Table 2, without any limitation due to the third-order RK method in this unsteady solution. Due to the locality of the jet stream, the 9th-order experiment ($k=8$) on a coarser grid resolves this test not as well as the 7th-order ($k=6$) experiment which explains the crossing of both error lines.

4.6. Perturbed jet stream

Supplementing the standard tests for atmospheric models based on SWE, [12] proposed a test describing a barotropic instability. The initial velocity field u is an axially symmetric westerly jet stream with the same axis as the Earth's rotation axis. As in Section 4.5, this jet stream includes strong meridional gradients and constitutes a rather local feature. Based on u a geopotential height Φ is derived in geostrophic balance to u. Additionally a small perturbation Φ_p is added, such that the initial condition for the test is the geopotential field $\Phi+\Phi_p$. As a consequence of the perturbation Φ_p, this experiment should not maintain the initial data. [12] give a detailed description of the barotropic instability developing within the jet stream from day four to day six.

At first, the model should be able to maintain the geostrophically balanced flow, as long as the initial perturbation does not lead to instabilities. Unlike for spectral models, this is not trivial for a model with a grid which is not aligned to the zonal flow. Fig. 11 shows the vorticity field after 4 days in a cutout of the global model domain for $k=2$ and two different model resolutions. Whereas a pronounced zonal wavenumber five is visible for $h=94$ km the experiment with the higher resolution $h=47$ km reduces the grid effect considerably. The same plot after 4 days is given in the upper plot of Fig. 12 for the model resoltuion $h=87$ km but polynomial order $k=6$. This "high-order" experiment seems to be more adequate to maintain the geostrophic structure of the flow avoiding a low wavenumber zonal wave. The two lower plots of Fig. 12 show the vorticity for $k=6$ and the resolutions 87 km and 44 km after 6 days. In both experiments the laminar flow structure looks very similar, which gives an indication for the experimental convergence in smooth regions. In contrast to this, the areas with strong gradients, where barotropic instabilities develop, show spurious oscillations. The same experiment has been performed with polynomial order $k=4$ and high model resolution $h=30$ km, see Fig. 13. Compared to the "low" and "high" order experiments in Figs. 11 and 12 the geostrophically balanced flow is maintained and the barotropic instabilities show only small spurious oscillations. Fig. 13 shows very good agreement with the inviscid run of [12] and the results in [40].

The discrete properties of the global invariants mass and energy are inspected. The experiments for all model resolutions achieve the conservation of mass up to machine precision. Fig. 14 shows the relative error for the global energy $\eta(E_h)$ as a

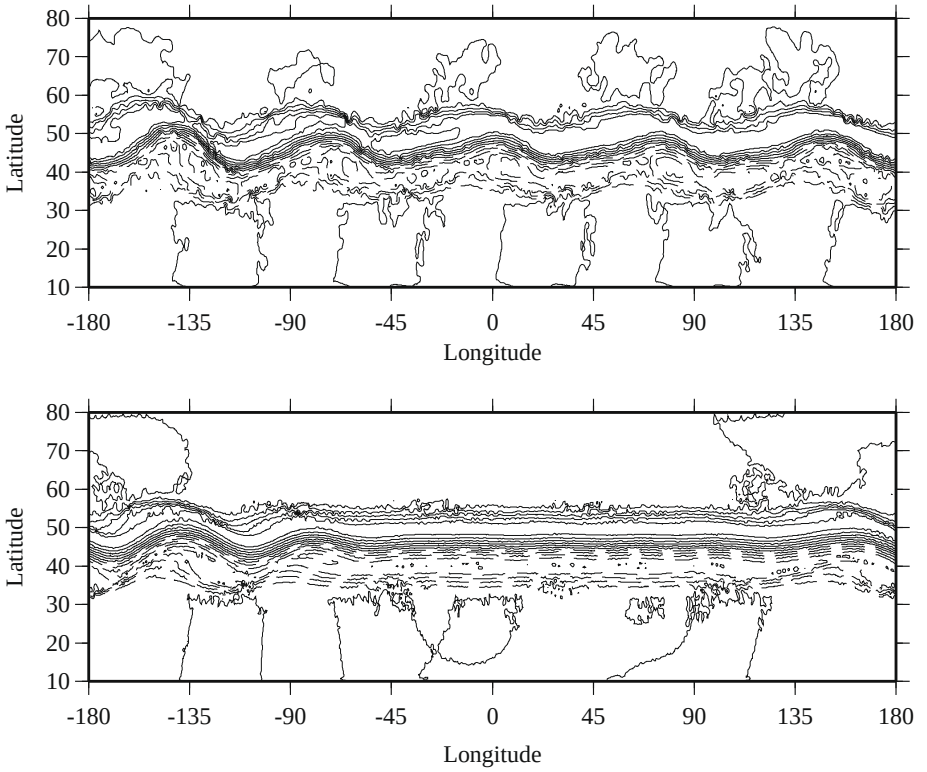

Fig. 11. Section 4.6 (perturbed jet stream), vorticity (contour interval $2\times10^{-5}s^{-1}$), day 4, $k=2$, top: $h=94$ km, bottom: $h=47$ km.

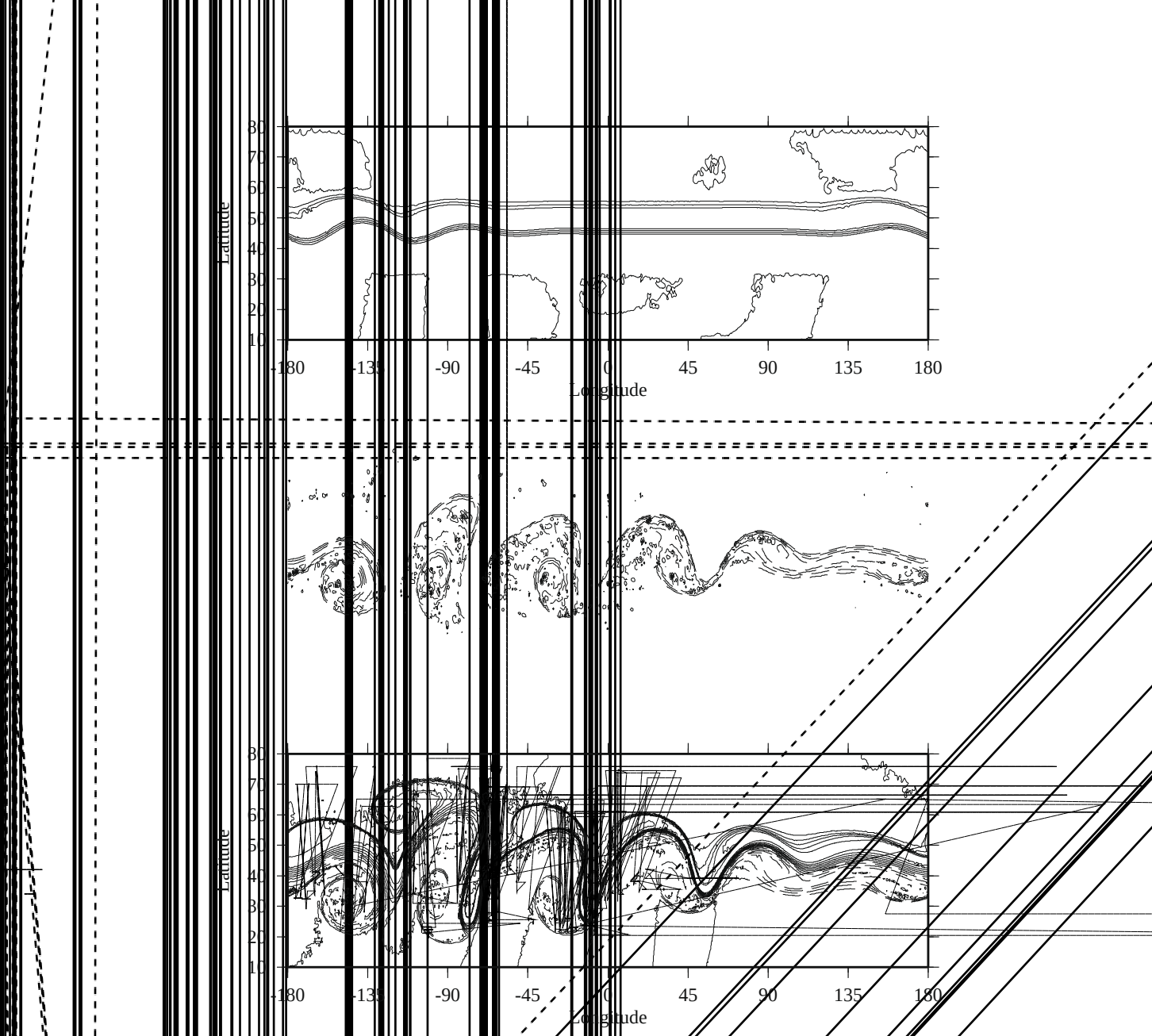

function of the model resolution h and simulation time T, respectively. The values of $h(L_h)$ at day 6 are in the range of $(2.9 \times 10^{-3}, 6 \times 10^{-4})$. That is, the error convergence is very similar to that in Section 4.2. Experimental convergence is obtained for a fixed polynomial orders k and decreasing Δx as well as for a fixed grid resolution Δx and increasing k. Between the days 1–3 the errors for $(h,k) = (44\ \text{km},6)$ and $(h,k) = (60\ \text{km},8)$ are even smaller than for $(h,k) = (30\ \text{km},4)$. The high-order experiments perform better, because the flow is very smooth and almost steady-state for the days 1–3. For the days 4–6 strong gradients develop in the regions of instability and benefit the low order ones.

5. Summary and outlook

A global model of the atmosphere has been developed based on the spherical shallow water equations and discretized by a Runge–Kutta discontinuous Galerkin method. The equations are formulated as a hyperbolic conservation law on the sphere, a two-dimensional surface in $\mathbb{R}^3$, using coordinate invariant differential operators.

[illegible] approach curved elements [illegible] spherical triangular grid. γ_F yields a two-dimensional representation of the tangential momentum fields, finally two [illegible] equations. γ_F denotes a reduction of variables compared to the three-

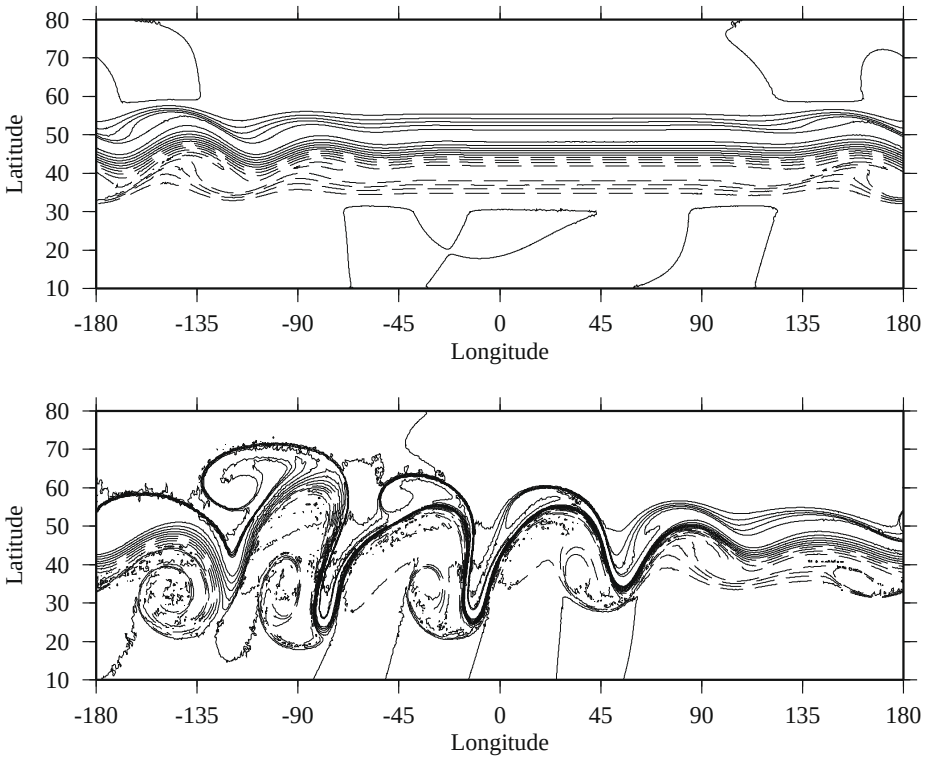

Fig. 13. Section 4.6 (perturbed jet stream), vorticity (contour interval $2 \times 10^{-5} s^{-1}$), $(h, k) = (30\text{ km}, 4)$, top: day 4, bottom: day 6.

dimensional representation in a Cartesian coordinate system. This point, although subtle, liberates the DG formulation from the grid, which means that any kind of conformal triangular (unstructured) grid can be used; this essentially represents an extension of the ideas put forth for quadrilateral grids by Sadourny [37], Ronchi et al. [33], and Rancic et al. [31] to triangular grids. Governed by an integral form of the conservation law the space-discrete discontinuous Galerkin method is obtained including a Rusanov numerical flux. An explicit third-order Runge–Kutta method (strong stability-preserving) is applied to the space-discrete system. The discrete method does not apply any kind of limiting or explicit smoothing such as diffusion and filter operators. Without a slope limiter no theoretical evidence for convergence can be expected (for scalar one-dimensional equations) but all numerical experiments give stable results. A shallow water model of the atmosphere is implemented based on the Runge–Kutta discontinuous Galerkin method completed by a time step control based on a CFL-condition. The model is validated using various numerical experiments.

Steady-state and unsteady analytical solutions of the nonlinear shallow water equations are considered. In all cases the model achieves experimental convergence to the known solution. Furthermore, for increasing polynomial order k, the error decreases significantly. For the steady-state solid body rotation and the unsteady jet stream the experimental orders of convergence are $O(\Delta x^{k+1})$. This convergence rate is achieved for the unsteady solid body rotation, only if $k \leqslant 4$. For higher orders k and very small errors the time step Δt limits the error (third-order Runge–Kutta method). This result of the presented atmospheric model demonstrates, that the model time step is restricted not only by a CFL-condition but by accuracy demands too. Further, a qualitative test regarding a barotropic instability within a perturbed jet stream is performed. In very good agreement to published results the experiment shows the evolution of a breaking barotropic wave after 6 days without generating spurious oscillations. The global energy error converges with increasing grid resolution as well as with increasing polynomial order. For all numerical experiments the anticipated mass conservation is achieved up to machine precision.

The presented results show the great potential of the Runge–Kutta discontinuous Galerkin method in a simplified atmospheric model. Thus, the application to the three-dimensional atmospheric equations, which form a hyperbolic system, seems to be warranted. The equation set for an atmospheric model does not have to be in hyperbolic form at all, either caused by constraints (hydrostatic, incompressible) or by complex driving forces (e.g. including higher order derivatives). If at all, the presented DG method can be applied in such situations only with further extensions (e.g. a local DG method). Furthermore, a three-dimensional atmospheric DG model will have to be compared to existing Galerkin models in terms of test cases and computational efficiency, see e.g. [11,14]. Further, the method demonstrates the application of local coordinate mappings, here spherical triangular coordinates, and its capacity to represent tangential momentum fields that are locally two-dimensional. Using the same technique for global atmospheric models in three-dimensional prismatic grids yields the useful decomposition into tangential and vertical components.

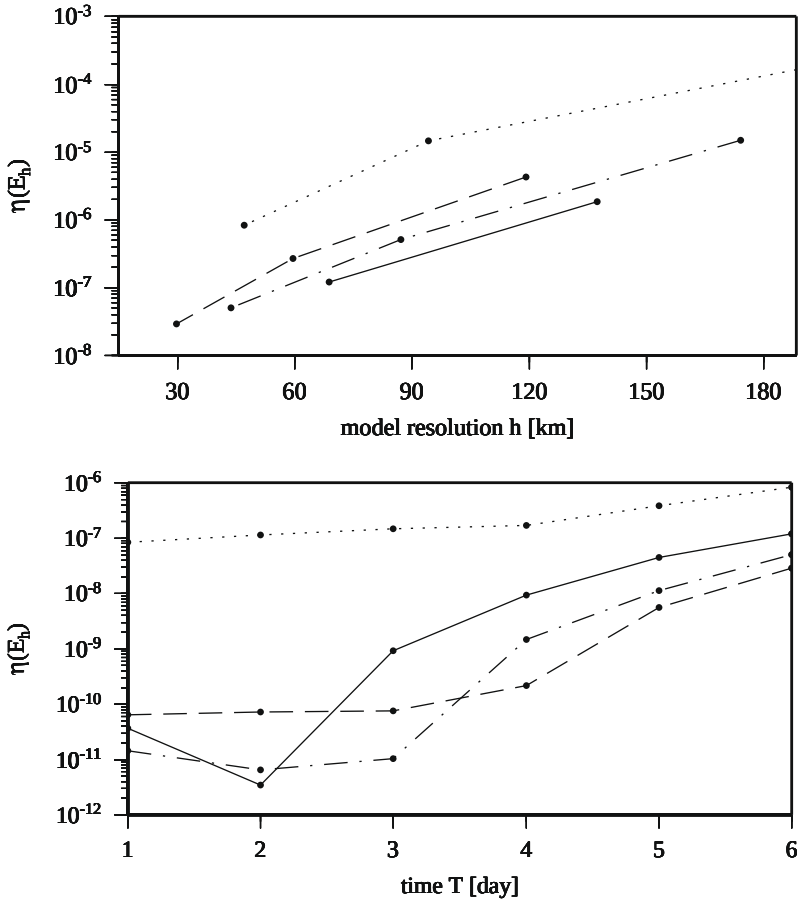

Fig. 14. Section 4.6 (perturbed jet stream), relative error for global energy $\eta(E_h)$, top: day 6 and $k = 2$ $(\cdots)$, $k = 4$ (–), $k = 6(-\cdot), k = 8$ (–), bottom: $(h, k) = (47\text{ km}, 2)$ $(\cdots)$, $(h, k) = (30\text{ km}, 4)$ (–), $(h, k) = (44\text{ km}, 6)(-\cdot), (h, k) = (69\text{ km}, 8)$ (–).

Acknowledgements

The authors gratefully acknowledge the support of the Office of Naval Research Global through the Grant N00014-07-1-4038. The second author also gratefully acknowledges the support of the Office of Naval Research through PE-0602435N.

Appendix. Manifolds

The spherical domain S is regarded as a two-dimensional C^1-manifold embedded in $\mathbb{R}^3$. Thus, the operators and Gauß' theorem on S are special cases of the standard definitions from differential geometry. Because the local representation of the operators and the integrals regarding a coordinate mapping γ are essential to the implementation of the model, these formulas are given below.

Let $f \in C^1(S)$ be a scalar function and $u \in C^1(S, \mathbb{R}^3)$ a vector field with $u(x) \in T_x(S)$. Further, for a fixed $x \in S$ let (τ_1, τ_2) be a orthonormal basis of $T_x(S)$. Then the spherical gradient and spherical divergence are defined by

$$\nabla_S f(x) = \sum_{i=1}^{2} \partial_{\tau_i} f(x) \tau_i, \ \operatorname{div}_S u(x) = \sum_{i=1}^{2} \tau_i \cdot \partial_{\tau_i} u(x)$$

with the directional derivative $\partial_\tau f(x) = \lim_{i\to\infty} \frac{f(x_i)-f(x)}{\varepsilon_i}$ for $\varepsilon_i \to 0$ and $\frac{x_i - x}{\varepsilon_i} \to \tau$. Then, for an open subset $E \subset S$ with smooth boundary a formulation of Gauß' theorem on S is

$$\int_E f \operatorname{div}_S u \, dx = -\int_E u \cdot \nabla_S f \, dx + \int_{\partial E} f u \cdot \nu_E \, d\sigma \tag{10}$$

with the outward normal vector $\nu_E(x) \in T_x(S)$ of E in the point x.

Let $D \subset \mathbb{R}^2$ open, $E \subset S$ open in S and $\gamma : D \to E$ a local coordinate mapping. γ generates the local coordinate system

$$b_i = \partial_{y_i}\gamma, \quad i = 1, 2$$

which is a basis of the tangential space $T_x(S)$. The condition $b_i \cdot b^j = \delta_i^j$ determines the dual basis (b^1, b^2) and it holds $b^i = \nabla_S y_i$. Gram's matrix (metric tensor), its inverse and Gram's determinant are defined by

$$g_{ij} = b_i \cdot b_j,\ g^{ij} = b^i \cdot b^j, \quad g = \det(g_{ij})_{i,j=1,2}.$$

Derivatives of the basis functions b_i are expressed using Christoffel symbols which fulfill the equations

$$\partial_{y_j} b^i = -\Gamma^i_{jk} b^k, \quad \Gamma^k_{ij} = \frac{g^{nk}}{2}(\partial_{y_i} g_{jn} + \partial_{y_j} g_{in} - \partial_{y_n} g_{ij}).$$

Then, for $y \in D$ the operators fulfill the local representations

$$\nabla_S f|_{\gamma(y)} = \sum_{i=1}^{2} [\partial_{y_i}(f \circ \gamma)]_y b^i,\ \operatorname{div}_S u|_{\gamma(y)} = \sum_{i=1}^{2} \frac{1}{\sqrt{g}} [\partial_{y_i} \sqrt{g}(u \circ \gamma) \cdot b^i]_y.$$

The face and line integrals satisfy the local representations

$$\int_E f \mathrm{d}x = \int_D \sqrt{g} f \circ \gamma \mathrm{d}y,\ \int_{\partial E} f \mathrm{d}\sigma = \int_{\partial D} \sqrt{g} |(b^1, b^2) \cdot \nu_D| f \circ \gamma \mathrm{d}\sigma \tag{11}$$

where ν_D is the unit normal on ∂D.

References

[1] J.R. Baumgardner, P.O. Frederickson, Icosahedral discretization of the two-sphere, SIAM J. Numer. Anal. 22 (1985) 1107–1115.
[2] J. Behrens, N. Rakowsky, W. Hiller, D. Handorf, M. Läuter, J. Päpke, K. Dethloff, amatos: parallel adaptive mesh generator for atmospheric and oceanic simulation, Ocean Model. 10 (2005) 171–183.
[3] P.G. Ciarlet, P.-A. Raviart, Interpolation theory over curved elements, with applications to finite element methods, Comput. Methods Appl. Mech. Engrg. 1 (1972) 217–249.
[4] B. Cockburn, C.-W. Shu, The Runge–Kutta local projection p^1-discontinuous-Galerkin finite element method for scalar conservation laws, Math. Mod. Num. Anal. 25 (1991) 337–361.
[5] B. Cockburn, C.-W. Shu, Runge–Kutta discontinuous Galerkin methods for convection-dominated problems, J. Sci. Comput. 16 (2001) 173–261.
[6] R. Cools, Monomial cubature rules since Stroud: a compilation – part 2, J. Comput. Appl. Math. 112 (1999) 21–27.
[7] R. Cools, P. Rabinowitz, Monomial cubature rules since Stroud: a compilation, J. Comput. Appl. Math. 48 (1993) 309–326.
[8] J. Côté, A Lagrange multiplier approach for the metric terms of semi-Lagrangian models on the sphere, Q.J.R. Meteorol. Soc. 114 (1988) 1347–1352.
[9] J. Dennis, A. Fournier, W.F. Spotz, A. St-Cyr, M.A. Taylor, S.J. Thomas, H. Tufo, High-resolution mesh convergence porperties and parallel efficiency of a spectral element atmospheric dynamical core, Int. J. High Perfor. Comput. Appl. 19 (2005) 225–235.
[10] V. Dolejsi, M. Feistauer, A semi-implicit discontinuous galerkin finite element method for the numerical solution of inviscid compressible flow, J. Comput. Phys. 198 (2004) 727–746.
[11] A. Fournier, M.A. Taylor, J.J. Tribbia, The spectral element atmosphere model (SEAM): high-resolution parallel computation and localized resolution of regional dynamics, Mon. Wea. Rev. 132 (2004) 726–748.
[12] J. Galewsky, R.K. Scott, L.M. Polvani, An initial-value problem for testing numerical models of the global shallow water equations, Tellus A 56 (2004) 429–440.
[13] F.X. Giraldo, Lagrange-Galerkin methods on spherical geodesic grids, J. Comput. Phys. 136 (1997) 197–213.
[14] F.X. Giraldo, Semi-implicit time-integrators for a scalable spectral element atmospheric model, Q.J.R. Meteorol. Soc. 131 (2005) 2431–2454.
[15] F.X. Giraldo, High-order triangle-based discontinuous Galerkin methods for hyperbolic equations on a rotating sphere, J. Comput. Phys. 214 (2006) 447–465.
[16] F.X. Giraldo, J.S. Hesthaven, T. Warburton, Nodal high-order discontinuous Galerkin methods for the spherical shallow water equations, J. Comput. Phys. 181 (2002) 499–525.
[17] F.X. Giraldo, T. Warburton, A nodal triangle-based spectral element method for the shallow water equations on the sphere, J. Comput. Phys. 207 (2005) 129–150.
[18] F.X. Giraldo, T. Warburton, A high-order triangular discontinuous Galerkin oceanic shallow water model, Int. J. Numer. Meth. Fluids 56 (2008) 899–925.
[19] S. Gottlieb, C.-W. Shu, E. Tadmor, Strong stability-preserving high-order time discretization methods, SIAM Rev. 43 (2001) 89–112.
[20] R. Heikes, D.A. Randall, Numerical integration of the shallow water equations on a twisted icosahedral grid. part i: basic design and results of tests, Mon. Wea. Rev. 123 (1995) 1862–1880.
[21] T. Heinze, A. Hense, The shallow water equations on the sphere and their Lagrange-Galerkin solution, Meteorol. Atmos. Phys. 81 (2002) 129–137.
[22] J.S. Hesthaven, From electrostatics to almost optimal nodal sets for polynomial interpolation in a simplex, SIAM J. Numer. Anal. 35 (1998) 655–676.
[23] L. Krivodonova, J. Xin, J.-F. Remacle, N. Chevaugeon, J.E. Flaherty, Shock detection and limiting with discontinuous Galerkin methods for hyperbolic conservation laws, Appl. Numer. Math. 48 (2004) 323–338.
[24] M. Läuter, D. Handorf, K. Dethloff, Unsteady analytical solutions of the spherical shallow water equations, J. Comput. Phys. 210 (2005) 535–553.
[25] M. Läuter, D. Handorf, N. Rakowsky, J. Behrens, S. Frickenhaus, M. Best, K. Dethloff, W. Hiller, A parallel adaptive barotropic model of the atmosphere, J. Comput. Phys. 223 (2007) 609–628.
[26] P. LeSaint, P.A. Raviart, On a finite element method for solving the neutron transport equation, in: C. de Boor (Ed.), Mathematical Aspects of Finite Elements in Partial Differential Equations, Academic Press, 1974, pp. 89–145.
[27] S.-J. Lin, R.B. Rood, An explicit flux-form semi-Lagrangian shallow-water model on the sphere, Q.J.R. Meteorol. Soc. 123 (1997) 2477–2498.
[28] J. Lyness, R. Cools, A survey of numerical cubature over triangles, Proc. Symp. Appl. Math. 48 (1994) 127–150.
[29] Detlev Müller, Angular-momentum budget of shallow waters on a rotating sphere, Phys. Rev. A 45 (8) (1992) 5545–5555.
[30] R.D. Nair, S.J. Thomas, R.D. Loft, A discontinuous Galerkin global shallow water model, Mon. Wea. Rev. 133 (2005) 876–888.
[31] M. Rancic, R.J. Purser, F. Mesinger, A global shallow water model using an expanded spherical cube: gnomonic versus conformal coordinates, Q.J.R. Meteorol. Soc. 122 (1996) 959–982.
[32] M. Restelli, F.X. Giraldo, A conservative discontinuous Galerkin sem-implicit formulation for the Navier-Stokes equations in nonhydrostatic mesoscale modeling, SIAM J. Sci. Comput., in review.

[33] C. Ronchi, R. Iacono, P.S. Paolucci, The cubed sphere: a new method for the solution of partial differential equations in spherical geometry, J. Comput. Phys. 124 (1996) 93–114.
[34] J.A. Rossmanith, A wave propagation method for hyperbolic systems on the sphere, J. Comput. Phys. 213 (2006) 629–658.
[35] J.A. Rossmanith, D.S. Bale, R.J. LeVeque, A wave propagation algorithm for hyperbolic systems on curved manifolds, J. Comput. Phys. 199 (2004) 631–662.
[36] S.J. Ruuth, R.J. Spiteri, Two barriers on strong-stability preserving time discretization methods, J. Sci. Comput. 17 (2002) 211–220.
[37] R. Sadourny, Conservative finite difference approximations of the primitive equations on quasi-uniform spherical grids, Mon. Wea. Rev. 100 (1972) 136–144.
[38] R. Sadourny, A. Arakawa, Y. Mintz, Integration of nondivergent barotropic vorticity equation with an icosahedral-hexagonal grid for sphere, Mon. Wea. Rev. 6 (1968) 351.
[39] C.-W. Shu, S. Osher, Efficient implementation of essentially non-oscillatory shock-capturing schemes, J. Comput. Phys. 77 (1988) 439–471.
[40] A. St-Cyr, C. Jablonowski, J.M. Dennis, H.M. Tufo, S.J. Thomas, A comparison of two shallow water models with non-conforming adaptive grids, Mon. Wea. Rev., in press.
[41] A.H. Stroud, Approximate Calculation of Multiple Integrals, Prentice-Hall, London, 1971.
[42] G.R. Stuhne, W.R. Peltier, New icosahedral grid-point discretizations of the shallow water equations on the sphere, J. Comput. Phys. 148 (1999) 23–58.
[43] P.N. Swarztrauber, The approximation of vector functions and their derivatives on the sphere, SIAM J. Numer. Anal. 18 (1981) 191–210.
[44] P.N. Swarztrauber, D.L. Williamson, J.B. Drake, The cartesian method for solving partial differential equations in spherical geometry, Dyn. Atmos. Oceans 27 (1997) 679–706.
[45] M. Taylor, J. Tribbia, M. Iskandarani, The spectral element method for the shallow water equations on the sphere, J. Comput. Phys. 130 (1997) 92–108.
[46] M.A. Taylor, B.A. Wingate, R.E. Vicent, An algorithm for computing Fekete points in the triangle, SIAM J. Numer. Anal. 38 (5) (2000) 1707–1720.
[47] J. Thuburn, Pv-based shallow water model on a hexagonal-icosahedral grid, Mon. Wea. Rev. 125 (1997) 2328–2347.
[48] H. Tomita, M. Tsugawa, M. Satoh, K. Goto, Shallow water model on a modified icosahedral geodesic grid by using spring dynamics, J. Comput. Phys. 174 (2001) 579–613.
[49] D.L. Williamson, Integration of barotropic flow on a spherical geodesic grid, Bull. Am. Meteor. Soc. 48 (1967) 589.
[50] D.L. Williamson, J.B. Drake, J.J. Hack, R. Jakob, P.N. Swarztrauber, A standard test set for numerical approximations to the shallow water equations in spherical geometry, J. Comput. Phys. 102 (1992) 211–224.